Analytical evaluation of output current ripple amplitude in three-phase three-level inverters

Gabriele Grandi[1], Jelena Loncarski[2], Obrad Dordevic[3]
[1]Dept. of Electrical Engineering, University of Bologna, Viale Risorgimento 2, 40136-Bologna, Italy
[2]Department of Engineering Sciences, Ångström Laboratory, Uppsala University, Sweden
[3]School of Engineering, Liverpool John Moores University, Byrom Street, Liverpool L3 3AF, UK
gabriele.grandi@unibo.it, jelena.loncarski@angstrom.uu.se, O.Dordevic@ljmu.ac.uk

Abstract—Nowadays, three-phase multilevel inverters are widely employed in medium and high-power applications, increasing the power ratings, improving the output voltage quality and reducing the conducted electromagnetic interferences. Despite of numerous pulse-width modulation (PWM) techniques have been developed for multilevel inverters, a detailed analysis of the output current ripple amplitude has not been reported yet. In this study, the peak-to-peak current ripple distribution over a fundamental period is analysed in details specifically for three-level three-phase voltage source inverters for both motor-load and grid-connected applications. In particular, the peak-to-peak amplitude of the current ripple is determined analytically as a function of the modulation index. The centred PWM strategy is considered in all the developments, implemented either by carrier-based or space vector (SV) PWM methods. With this modulation, the dc bus utilisation is maximised in a simple and effective way, and a nearly-optimal behaviour is obtained to minimise the current ripple rms. The results obtained in different cases and sub-cases identified in the proposed analytical approach are verified by experimental tests with reference to three-phase three-level neutral-point clamped configuration.

I. Introduction

Multilevel inverters became more and more popular in last decades, because of the increased power ratings, improved output voltage waveforms, and reduced electromagnetic interference emission. In particular, power switches are properly combined leading to a structure capable of reaching high output voltage amplitudes by using standard low-voltage components [1].

Among multilevel converters, three-level pulse-width modulation (PWM) voltage source inverters (VSIs) are the viable converters for many high-power applications, both grid-connected and motor-load. Compared with traditional two-level inverters, three-level inverters have half of the voltage stress on switching devices for the same maximum output voltage and generate lower harmonics for the same switching frequency. Most popular three-level configurations are cascaded connection of single-phase inverters (H-bridge) and neutral-point clamped (NPC) inverters, represented in Figs. 1(a) and (b), respectively.

Pre-print. Final version of this paper appears inIET Digital Library (http://digital-library.theiet.org/content/journals/iet-pel) and IEEE Xplore Digital Library (http://ieeexplore.ieee.org/Xplore/guesthome.jsp).

The performance of a three-level inverter depends on its modulation strategy. There have been many three-level PWM techniques developed in last decades [2–6]. Generally these techniques can be classified into two categories: carrier-based modulation (CB-PWM), and space vector modulation (SV-PWM). For CB-PWM each phase reference voltage is compared with two identically shaped but offset triangle carrier waveforms, leading to so-called phase disposition (PD) modulation technique. The frequency of these carriers defines the switching frequency, and their amplitude is the same as dc-link voltage, eventually in per units. A typical SV-PWM scheme uses the nearest three vectors algorithm to approximate the desired output voltage vector. During each switching period, the triangle in which the reference vector lies is traversed forth and back once. Beginning and ending states of this traverse correspond to the same space vector, that is called pivot vector. These two redundant switching states are called pivot states. In most continuous modulation strategies for a three-level inverter, the switching sequence starts from first pivot state, goes to the second and symmetrically comes back to the first.

CB-PWM strategies are widely adopted because of their inherent simplicity and reduced computational requirements compared with SV-PWM, with the possibility of implementation on industrial digital signal processors without the need of additional hardware logics such as field-programmable gate array. Furthermore, it is proved that CB-PWM and SV-PWM strategies for multilevel inverters are equivalent. A proper common-mode injection into the modulating signals of the CB-PWM leads to the same output voltages as in SV-PWM. On the other hand, the CB-PWM can be equivalently realised by SV-PWM through proper sharing of dwell times among the redundant switching states. In particular, the so-called centred PWM (CPWM) obtained by splitting the dwell times of redundant states into equal parts offers lower harmonic distortion in output currents and almost easy implementation with both CB-PWM and SV-PWM techniques [7–13].

The output current ripple affects the noise and loss in both the PWM converter and the load, and it should be minimised to improve the system efficiency. In general, the impact of PWM techniques on the current ripple should be understood to further develop the modulation strategy. Various PWM schemes for three-level VSIs with improved output voltage waveforms have been proposed in last decades, but the effects of these modulation strategies on the peak-to-peak output current ripple has not been emphasised yet. In [14], the current ripple trajectory in $\alpha-\beta$ coordinates for the case of dual-inverter-fed open-end winding load configuration, operating as three-level inverter, is shown. However, the emphasis was on current ripple rms.

The analysis of the output current ripple amplitude in three-phase two-level PWM inverters has been recently introduced in [15]. A more detailed investigation is presented in [16], also introducing simple and effective expressions to determine the maximum amplitude of the peak-to-peak current ripple in the fundamental period. The extension to multiphase inverters is given in [17] for five-phase VSI and in [18] for seven-phase VSI. A comparison considering the different phase number is shown in [19]. In general, the evaluation of peak-to-peak current ripple amplitude is useful to

determine the dead-time output voltage distortion in case of high ripple currents with multiple zero-crossing. This analysis has been presented in [20] for the case of traditional three-phase two-level inverters. In [21, 22] an adaptive compensation is proposed to reduce the effects of the current ripple on the dead-time voltage distortion, but the evaluation of the current ripple amplitude was not properly investigated. The knowledge of the current ripple amplitude is also useful to compare PWM schemes with hysteresis current controllers, for two-level inverters [23–25], and for multilevel inverters [26–28]. Furthermore, in order to set current thresholds of protection systems and for the design of power components, the absolute current peak can be determined by combining the evaluation of peak-to-peak current ripple amplitude with the fundamental current component.

A detailed analysis of peak-to-peak current ripple amplitude is developed in this paper for three-phase three-level PWM inverters. Reference is made to centred and symmetrical switching patterns, able to minimise the current ripple rms. The current ripple analysis is carried out for a balanced three-phase system consisting of series RL impedance and ac back emf (RLE), representing both motor-loads and grid-connected applications. The evaluation of the current ripple distribution over a fundamental period is carried out as function of the modulation index. The analytical developments are verified by experimental tests considering an induction motor-load, with reference to the NPC three-level inverter configuration represented in Fig. 1(b).

II. Basic Equations and Inverter Modulation

A. Basic voltage and current equations

Basic voltage equation for each phase of a three-phase RLE load (Fig. 1), representing both ac motors and grid connected applications, is

$$v(t) = R\,i(t) + L\frac{di}{dt} + v_g(t)\,. \tag{1}$$

Averaging (1) and introducing the current variation $\Delta i = i(T_s) - i(0)$ in the switching period T_s gives

$$\bar{v}(T_s) = R\,\bar{i}(T_s) + \frac{L\,\Delta i}{T_s} + \bar{v}_g(T_s)\,, \tag{2}$$

The alternating voltage $\tilde{v}(t)$ is defined as the difference between instantaneous and average voltage components as

$$\tilde{v}(t) = v(t) - \bar{v}(T_s)\,. \tag{3}$$

Introducing (1) and (2) in (3) gives

$$\tilde{v}(t) = R\left[i(t) - \bar{i}(T_s)\right] + L\left[\frac{di}{dt} - \frac{\Delta i}{T_s}\right] + \left[v_g(t) - \bar{v}_g(T_s)\right] \tag{4}$$

Pre-print. Final version of this paper appears inIET Digital Library (http://digital-library.theiet.org/content/journals/iet-pel) and IEEE Xplore Digital Library (http://ieeexplore.ieee.org/Xplore/guesthome.jsp).

The expression of alternating voltage (4) can be further simplified since the first and the third (last) term are negligible with respect to the second term [16-18], leading to

$$\tilde{v}(t) \cong L\left[\frac{di}{dt} - \frac{\Delta i}{T_s}\right] \tag{5}$$

By integrating (5), the current variation in sub-period [0 – t] can be calculated as

$$\Delta i(t) \cong \frac{1}{L}\int_0^t \tilde{v}(t)dt + \frac{t}{T_s}\Delta i \tag{6}$$

Finally, the instantaneous current ripple $\tilde{i}(t)$ can be defined on the basis of (6), according to Fig. 2

$$\tilde{i}(t) = \Delta i(t) - \frac{t}{T_s}\Delta i \cong \frac{1}{L}\int_0^t \tilde{v}(t)dt\,. \tag{7}$$

An example of the behaviour of voltage and current in the whole switching period is given in Fig. 2. Note that the current ripple (7) corresponds to the difference between the instantaneous current value and its fundamental component. The peak-to-peak current ripple amplitude $\tilde{i}_{pp}$ is defined as the range of (7) in the switching period

$$\tilde{i}_{pp} = max\left\{\tilde{i}(t)\right\}_0^{T_s} - min\left\{\tilde{i}(t)\right\}_0^{T_s}\,. \tag{8}$$

B. Space vector analysis and PWM equations

The analysis of three-phase inverters by the space vector transformation leads to better understanding and more simple calculation of voltage levels and corresponding application times. In the case of a three-level inverter, the output voltage vector can be written similarly to the corresponding two-level inverter, considering the switching states of the k-th inverter phase as S_k = [-1,0, 1] (in the following are summarized as {– o +}):

$$\boldsymbol{v} = \frac{2}{3}V_{dc}\left[S_1 + S_2\boldsymbol{\alpha} + S_3\boldsymbol{\alpha}^2\right]. \tag{9}$$

being $\boldsymbol{\alpha} = exp(j2\pi/3)$.

Fig. 3(a) shows the output voltage space vectors corresponding to all possible switch configurations. In three-level inverters, the redundancy implies availability of multiple switching states to produce a given voltage vector. There is redundancy in zero vector (possible states are {+ + +}, {o o o}, and {– – –}), and in all the vectors of magnitude 2/3 V_{dc} (pivot vectors, red dots in Fig. 3) with two possible states. The three nearest voltage vectors are used to synthesize the reference output voltage vector $\boldsymbol{v}^*$ in a switching period. For sinusoidal balanced output voltages, the reference output voltage vector is $\boldsymbol{v}^* = V^* exp(j\vartheta)$, being $V^* = m\,V_{dc}$ and $\vartheta = \omega t$, m the modulation index and V_{dc} the dc bus voltage.

Pre-print. Final version of this paper appears inIET Digital Library (http://digital-library.theiet.org/content/journals/iet-pel) and IEEE Xplore Digital Library (http://ieeexplore.ieee.org/Xplore/guesthome.jsp).

The voltage space vector diagram of three-level inverter appears to be a hexagon, consisting of 6 main triangles, numbered I–VI in Fig. 3, 12 outer triangles, 6 intermediate and 6 inner triangles. SV modulation is quarter-wave symmetric, so the analysis can be restricted to the first quadrant, i.e. phase angle ϑ ranging between 0° and 90°. The hexagon is divided into 6 diamond-shaped regions, bordered by red lines in Fig. 3(a), each one with its pivot vector. The switching sequence begins and ends with the pivot vector, making the role of pivot vector in three-level VSIs similar to the role of zero vector in case of two-level VSIs. In centred space vector PWM the application time of pivot vector is shared in two equal parts for pivot states. In this way, a nearly-optimal modulation minimising the current ripple rms can be achieved, as described in [8, 10].

The multilevel modulation strategy is described with reference to Fig. 3(b) for the first main triangle. The nearest pivot vector $\boldsymbol{v}_p$ is subtracted from the reference voltage vector $\boldsymbol{v}^*$ to obtain the residual reference vector $\boldsymbol{v}_\gamma$, that can be synthesized by applying the same procedure as for two-level inverters in the corresponding triangle (I-3a in Fig. 3). Application times t_k are defined by duty-cycles δ_1, δ_2, and δ_p, and switching period T_s, being $\delta_k = t_k/T_s/2$. Duty-cycles are given in Table 1 for all the triangles named in Fig. 3(a) (first quadrant), by introducing the normalized reference voltages u_α and u_β defined as:

$$\begin{cases} u_\alpha = \dfrac{v_\alpha}{V_{dc}} = m\cos\vartheta \\ u_\beta = \dfrac{v_\beta}{V_{dc}} = m\sin\vartheta \end{cases} \tag{10}$$

being v_α and v_β the real and imaginary components of $\boldsymbol{v}^*$, as represented in Fig. 3(b). Note that the modulation limit is $m \le m_{\max} = 2/\sqrt{3} \approx 1.155$.

From the point of view of CB-PWM, the centered modulation is obtained by adding a common-mode signal to the three-phase sinusoidal reference waveforms v_k^*. In this way, the resulting modulating signals $\hat{v}_k^*$ are able to equally share the application times of redundant states [8], [10]:

$$\hat{v}_k^* = v_k^* - \frac{\left[\max(v_1,v_2,v_3)+\min(v_1,v_2,v_3)\right]}{2} + \frac{V_{dc}}{2} - \frac{\left[\max(v_1'',v_2'',v_3'')+\min(v_1'',v_2'',v_3'')\right]}{2}, \tag{11}$$

where k = 1, 2, 3, and v_1", v_2", v_3" stand for:

$$v_k'' = \mathrm{mod}\left\{ v_k^* - \frac{\left[\max(v_1,v_2,v_3)+\min(v_1,v_2,v_3)\right]}{2} + V_{dc},\, V_{dc} \right\}. \tag{12}$$

An alternative solution to implement the centered modulation with the CB-PWM is described in [11]. In this case, the common-mode signal to be injected is defined according to Table 2, with reference to minimum, middle, and maximum values of reference voltages v_1^*, v_2^*, v_3^* (Min, Mid, and Max, respectively). A simplified and effective method has been recently introduced in [29].

III. EVALUATION OF CURRENT RIPPLE AMPLITUDE

In the considered case of sinusoidal balanced currents, the three-phase system is symmetric and only one phase can be analyzed. Considering the first phase, the variables are given by extracting the real part of the corresponding space vectors, that is its projection on the real axes. If the reference voltage is within the modulation limits, i.e., the reference space vector $\boldsymbol{v}^*$ lies within the outer hexagon, the average inverter output voltage (first phase) is given by

$$\bar{v}\ (T_s) = v^* = Re\{\boldsymbol{v}^*\} = V^* \cos\vartheta = V_{dc}\, m \cos\vartheta\,. \tag{13}$$

The instantaneous output phase voltage $v(t)$ can be expressed by the switching states. For the first phase it can be calculated as the real part of the output voltage vector (9), leading to:

$$v = V_{dc}\left[S_1 - \frac{1}{3}(S_1 + S_2 + S_3)\right]. \tag{14}$$

By introducing (13) and (14) in (3), the alternating output voltage component is:

$$\tilde{v}(t) = V_{dc}\left[S_1 - \frac{1}{3}\left(S_1 + S_2 + S_3\right)\right] - V_{dc}\, m \cos\vartheta\,. \tag{15}$$

The current ripple evaluation in the first quadrant, $0 < \vartheta < \pi/2$, can be carried out by considering the three main sectors $0 \le \vartheta \le \pi/6$, $\pi/6 \le \vartheta \le \pi/3$, and $\pi/3 \le \vartheta \le \pi/2$, taking into account all the sub-cases matching the coloured areas represented in Fig. 3(c), as described in the following sub-sections.

The alternating voltage and the current ripple are summarized with separate diagrams for inner, intermediate, and outer triangles, from Fig. 4 to Fig. 6, respectively. In all cases, two different current ripple peaks are observed in the switching period. Owing to the modulation symmetry, positive and negative peaks have the same magnitude. In general, for each sector and for the different ranges of $m \cos\vartheta$, it will be shown that one peak results always to be equal or bigger than the other, by observing both current slopes and the corresponding application times.

A. Ripple analysis in the first sector

In the first sector, $0 \le \vartheta \le \pi/6$, five different sub-cases are identified, related to the different coloured regions in Fig. 3(c). Instantaneous output voltage $v(t)$, current ripple $\tilde{i}$ and peak-to-peak value $\tilde{i}_{pp}$ in the sub-case $0 \le m \cos\vartheta \le 1/3$, are presented in diagram ❶ of Fig. 4(a), corresponding to the left yellow area of the triangle I-1a in Fig. 3(c).

Introducing (7) in (8), and taking into account of (15), the switch configurations {o – –} and {o o –}, with the corresponding duty-cycles $\delta_p/2$ and δ_2, can be considered to evaluate $\tilde{i}_{pp}$, according to Fig. 4(a), leading to

$$\tilde{i}_{pp} = \frac{V_{dc} T_s}{L}\left\{\left(\frac{2}{3} - m\cos\vartheta\right)\frac{\delta_p}{2} + \left(\frac{1}{3} - m\cos\vartheta\right)\delta_2\right\}. \tag{16}$$

The peak-to-peak current ripple amplitude can be normalized by introducing $r(m,\vartheta)$ as

$$\tilde{i}_{pp} = \frac{V_{dc}T_s}{2L} r(m,\vartheta) . \tag{17}$$

On the basis of the duty-cycles given in Table 1, and introducing u_α, u_β, the normalized current ripple $r(m,\vartheta)$ for this sub-case of triangle I-1a becomes

$$\begin{aligned} r(m,\vartheta) &= \left(\frac{2}{3} - m\cos\vartheta\right)\delta_p + 2\left(\frac{1}{3} - m\cos\vartheta\right)\delta_2 = \\ &= \frac{3}{2}\left(\frac{2}{3} - u_\alpha\right)\left(u_\alpha - \frac{1}{\sqrt{3}}u_\beta\right) + 2\left(\frac{1}{3} - u_\alpha\right)\sqrt{3}u_\beta \end{aligned} . \tag{18}$$

The sub-case $m\cos\vartheta > 1/3$, corresponding to the right orange region of triangle I-1a in Fig. 3(c), is depicted in diagram ❷ of Fig. 4(a). In this case $\tilde{i}_{pp}$ can be evaluated considering the switch configuration {o − −}, with the corresponding duty- cycle $\delta_p/2$, leading to

$$\tilde{i}_{pp} = \frac{V_{dc}T_s}{L}\left\{\left(\frac{2}{3} - m\cos\vartheta\right)\frac{\delta_p}{2}\right\} . \tag{19}$$

Introducing the expression for δ_p given in Table 1 and normalizing, the current ripple becomes

$$r(m,\vartheta) = \frac{3}{2}\left(\frac{2}{3} - u_\alpha\right)\left(u_\alpha - \frac{1}{\sqrt{3}}u_\beta\right) . \tag{20}$$

The sub-cases $m\cos\vartheta \le 2/3$ and $m\cos\vartheta > 2/3$, both corresponding to the purple triangle I-2a in Fig. 3(c), are depicted in diagrams ❶ and ❷ of Fig. 5(a). In both cases the switch configurations {+ o o} and {+ o −}, with the corresponding duty-cycles $\delta_p/2$ and δ_1, can be considered to evaluate $\tilde{i}_{pp}$, leading to

$$\tilde{i}_{pp} = \frac{V_{dc}T_s}{L}\left\{\left(\frac{2}{3} - m\cos\vartheta\right)\frac{\delta_p}{2} + \left(1 - m\cos\vartheta\right)\delta_1\right\} . \tag{21}$$

Introducing the expression for δ_p and δ_1 given in Table 1 and normalizing, the current ripple becomes

$$r(m,\vartheta) = \left(\frac{2}{3} - u_\alpha\right)\left(1 - \sqrt{3}u_\beta\right) + 2\left(1 - u_\alpha\right)\left[\frac{3}{2}\left(u_\alpha + \frac{1}{\sqrt{3}}u_\beta\right) - 1\right] . \tag{22}$$

The sub-case $2/3 \le m\cos\vartheta \le 1$, corresponding to the blue area of triangle I-3a in Fig. 3(c), is presented in diagram ❶ of Fig. 6(a). In this case, the switch configuration {o − −} with the corresponding duty-cycle $\delta_p/2$ can be considered to evaluate $\tilde{i}_{pp}$, leading to

$$\tilde{i}_{pp} = \frac{V_{dc}T_s}{L}\left\{\left(m\cos\vartheta - \frac{2}{3}\right)\frac{\delta_p}{2}\right\} . \tag{23}$$

Introducing the expression for δ_p given in Table 1 and normalizing, the current ripple becomes

Pre-print. Final version of this paper appears inIET Digital Library (http://digital-library.theiet.org/content/journals/iet-pel) and IEEE Xplore Digital Library (http://ieeexplore.ieee.org/Xplore/guesthome.jsp).

$$r(m,\vartheta)=\left(u_\alpha-\frac{2}{3}\right)\left[2-\frac{3}{2}\left(u_\alpha+\frac{1}{\sqrt{3}}u_\beta\right)\right]. \tag{24}$$

The sub-case $1 \le m\cos\vartheta \le m_{\max}\cos\vartheta < 4/3$, corresponding to the green area of triangle I-3a in Fig. 3(c), is presented in diagram ❷ of Fig. 6(a). In this case the switch configurations {+ o o} and {+ o −}, with the corresponding duty-cycles $\delta_p/2$, and δ_1, can be considered to evaluate $\tilde{i}_{pp}$, leading to

$$\tilde{i}_{pp}=\frac{V_{dc}T_s}{L}\left\{\left(m\cos\vartheta-\frac{2}{3}\right)\frac{\delta_p}{2}+(m\cos\vartheta-1)\delta_1\right\}. \tag{25}$$

Introducing the expression for δ_p and δ_1 given in Table 1 and normalizing, the current ripple becomes

$$r(m,\vartheta)=\left(u_\alpha-\frac{2}{3}\right)\left[2-\frac{3}{2}\left(u_\alpha+\frac{1}{\sqrt{3}}u_\beta\right)\right]+2(u_\alpha-1)\sqrt{3}u_\beta. \tag{26}$$

B. Ripple analysis in the second sector

In the second sector, $\pi/6 \le \vartheta \le \pi/3$, three different sub-cases are identified, related to the three coloured regions in Fig. 3(c). The sub-cases $0 \le m\cos\vartheta \le 1/3$ and $m\cos\vartheta > 1/3$, both corresponding to the purple triangle I-1b in Fig. 3(c), are presented in diagrams ❶ and ❷ of Fig. 4(b). According to this figure, the switch configurations {+ + o} and {+ o o}, with the corresponding duty-cycles $\delta_p/2$ and δ_1, can be considered to evaluate $\tilde{i}_{pp}$ for both sub-cases, leading to

$$\tilde{i}_{pp}=\frac{V_{dc}T_s}{L}\left\{\left(\frac{1}{3}-m\cos\vartheta\right)\frac{\delta_p}{2}+\left(\frac{2}{3}-m\cos\vartheta\right)\delta_1\right\}. \tag{27}$$

Introducing the expressions for δ_p and δ_1 given in Table 1 and normalizing, the current ripple becomes

$$r(m,\vartheta)=\left(\frac{1}{3}-u_\alpha\right)\sqrt{3}u_\beta+3\left(\frac{2}{3}-u_\alpha\right)\left(u_\alpha-\frac{1}{\sqrt{3}}u_\beta\right). \tag{28}$$

The sub-cases $m\cos\vartheta \le 2/3$, corresponding to the blue area of triangles I-2b and I-3b in Fig. 3(c), are presented in diagram ❶ of Fig. 5(b) and in diagram ❶ of Fig. 6(b). For both sub-cases the switch configuration {o o −} with the corresponding duty-cycle $\delta_p/2$, can be considered to evaluate $\tilde{i}_{pp}$, leading to

$$\tilde{i}_{pp}=\frac{V_{dc}T_s}{L}\left\{\left(m\cos\vartheta-\frac{1}{3}\right)\frac{\delta_p}{2}\right\}. \tag{29}$$

Introducing the expressions for δ_p given in Table 1 and normalizing, the current ripple becomes

$$r(m,\vartheta)=\left(u_\alpha-\frac{1}{3}\right)\left[1-\frac{3}{2}\left(u_\alpha-\frac{1}{\sqrt{3}}u_\beta\right)\right], \text{ for triangle I-2b,} \tag{30}$$

$$r(m,\vartheta)=\left(u_\alpha-\frac{1}{3}\right)\left[2-\frac{3}{2}\left(u_\alpha+\frac{1}{\sqrt{3}}u_\beta\right)\right],\ \text{for triangle I-3b.} \tag{31}$$

The sub-cases $m\cos\vartheta > 2/3$, corresponding to the yellow area of triangles I-2b and I-3b in Fig. 3(c), are presented in diagram ❷ of Fig. 5(b) and in diagram ❷ of Fig. 6(b). In these sub-cases the switch configurations {+ + o} and {+ o o} for triangle I-2b, and {+ + o} and {+ + −} for triangle I-3b, with the corresponding duty-cycles $\delta_p/2$ and δ_1 for both, can be considered to evaluate $\tilde{i}_{pp}$, leading to

$$\tilde{i}_{pp}=\frac{V_{dc}T_s}{L}\left\{\left(m\cos\vartheta-\frac{1}{3}\right)\frac{\delta_p}{2}+\left(m\cos\vartheta-\frac{2}{3}\right)\delta_1\right\}. \tag{32}$$

Introducing the expressions for δ_p and δ_1 given in Table 1 and normalizing, the current ripple becomes

$$r(m,\vartheta)=\left(u_\alpha-\frac{1}{3}\right)\left[1-\frac{3}{2}\left(u_\alpha-\frac{1}{\sqrt{3}}u_\beta\right)\right]+2\left(u_\alpha-\frac{2}{3}\right)\left(1-\sqrt{3}u_\beta\right),\ \text{for triangle I-2b,} \tag{33}$$

$$r(m,\vartheta)=\left(u_\alpha-\frac{1}{3}\right)\left[2-\frac{3}{2}\left(u_\alpha+\frac{1}{\sqrt{3}}u_\beta\right)\right]+2\left(u_\alpha-\frac{2}{3}\right)\left(\sqrt{3}u_\beta-1\right),\ \text{for triangle I-3b.} \tag{34}$$

C. Ripple analysis in the third sector

In the third sector, $\pi/3 \le \vartheta \le \pi/2$, two different sub-cases are identified, related to the two coloured regions on Fig. 3(c). The first sub-cases considering triangles II-1a and II-2a, corresponding to the yellow area in Fig. 3(c), are presented in diagram ❶ of Fig. 4(c), and in diagram ❶ of Fig. 5(c). In these sub-cases the switch configurations {+ + o} for triangle II-1a, and {o o −} for triangle II-2a, with the corresponding duty-cycle $\delta_p/2$ for both, can be considered to evaluate $\tilde{i}_{pp}$, leading to

$$\tilde{i}_{pp}=\frac{V_{dc}T_s}{L}\left\{\left(\frac{1}{3}-m\cos\vartheta\right)\frac{\delta_p}{2}\right\}. \tag{35}$$

Introducing the expressions for δ_p given in Table 1 and normalizing, the current ripple becomes

$$r(m,\vartheta)=\frac{3}{2}\left(\frac{1}{3}-u_\alpha\right)\left(u_\alpha+\frac{1}{\sqrt{3}}u_\beta\right),\ \text{for triangle II-1a,} \tag{36}$$

$$r(m,\vartheta)=\left(\frac{1}{3}-u_\alpha\right)\left[1-\frac{3}{2}\left(\frac{1}{\sqrt{3}}u_\beta-u_\alpha\right)\right],\ \text{for triangle II-2a.} \tag{37}$$

The second sub-cases are considering triangle II-3a, corresponding to the purple triangle in Fig. 3(c), are presented in diagrams ❶ and ❷ of Fig. 6(c). In both sub-cases the switch configurations {+ + o} and {o + −}, with the corresponding the duty-cycles $\delta_p/2$ and δ_1, can be considered to evaluate $\tilde{i}_{pp}$, leading to

$$\tilde{i}_{pp} = \frac{V_{dc}T_s}{L}\left\{\left(m\cos\vartheta - \frac{1}{3}\right)\frac{\delta_p}{2} + m\cos\vartheta\delta_1\right\}. \quad (38)$$

Introducing the expression for δ_p and δ_1 given in Table 1 and normalizing, the current ripple becomes

$$r(m,\vartheta) = \left(u_\alpha - \frac{1}{3}\right)\left(2 - \sqrt{3}u_\beta\right) + 3u_\alpha\left(\frac{1}{\sqrt{3}}u_\beta - u_\alpha\right). \quad (39)$$

IV. RESULTS

A. *Diagrams of peak-to-peak current ripple amplitude*

The behaviour of the peak-to-peak current ripple amplitude in the fundamental period (first quadrant) is summarized in Fig. 7. In particular, the normalized current ripple $r(m,\vartheta)$ defined by (17) is presented.

Fig. 7(a) shows $r(\vartheta)$ in the cases of m = 1/3, 1/2, 2/3, 1, and $2/\sqrt{3}$ ($m_{\max}$), corresponding to dashed circles (blue) in Fig. 3(c). The crossing of the three main sectors are visible for modulation indexes 1/3, 1/2, and 2/3. For m = 1 six different regions are visible, whereas four different regions can be distinguished for the maximum modulation index ($2/\sqrt{3}$). All these regions correspond to the different coloured areas in Fig. 3(c).

In Fig. 7(b) the coloured map of $r(m,\vartheta)$ in the first quadrant of the normalized output voltage vector (u_α - u_β plane) is presented. The current ripple goes to zero in the surroundings of m = 0, being mainly applied only the null vector. The same behaviour can be noticed around all the output vectors, since at their tip the output voltage perfectly matches the reference voltage, and the current ripple becomes zero. The map shows a general continuous distribution of the current ripple amplitude. The only discontinuity is observed across the phase angle $\pi/6$ (red line in Fig. 7(b)), because of the change of pivot vector (two red dots).

By observing Fig. 7 it can be noticed that the maximum current ripple amplitude is almost constant for intermediate modulation indexes, that is, $m \approx [0.1 – 1]$, ranging around the value 0.2, leading to the simplified expression

$$r^{max} \approx 0.2 \quad \text{or} \quad \tilde{i}_{pp}{}^{max} \approx \frac{V_{dc}T_s}{10L} \qquad \text{in the approximate range } 0.1 \le m \le 1 \quad (40)$$

B. *Experimental verification*

Experimental results are carried out to verify the peak-to-peak current ripple amplitude calculated by the proposed analytical developments. Custom-made three-level NPC inverter was used, as shown in Fig. 1(b). Power switches are Semikron SKM50GB12T4 IGBT modules, and clamping diodes are Semikron SKKD 46/12. The dSpace ds1006 hardware has been employed for the real-time implementation of the algorithm. The experiments have been done by feeding a three-phase symmetrical induction motor (not loaded). A picture of the experimental setup is given in Fig.

Pre-print. Final version of this paper appears inIET Digital Library (http://digital-library.theiet.org/content/journals/iet-pel) and
IEEE Xplore Digital Library (http://ieeexplore.ieee.org/Xplore/guesthome.jsp).

8(a). Main motor parameters (all referred to stator) are: stator resistance R_s = 2.4 Ω, rotor resistance R_r' = 1.6 Ω, stator leakage inductance L_{ls} = 12 mH, rotor leakage inductance L_{lr}' = 12 mH, magnetizing inductance L_m = 300 mH, pole pairs p = 2. According to the model of induction motor for higher order harmonics, which are determining the current ripple, the equivalent inductance $L = L_{ls} + L_{lr}' = 24$ mH is considered for the ripple evaluation.

The total dc voltage ($2V_{dc}$), provided from the external dc source Sorensen SGI 600/25, was 600V. Switching frequency was set to 2.1 kHz and the inverter's dead time of 6 μs (not compensated) is implemented in the hardware. Fundamental frequency was kept at 50 Hz for easier comparison with analytical developments. The nearly-optimal centered space vector PWM presented in Section II B is implemented by the equivalent PD carrier-based PWM on the basis of the modulating signals defined by (11) and [29].

Tektronix oscilloscope MSO2014 with current probe TCP0030 was used for measurements, and the built-in noise filter (cut-off frequency f_c = 600 kHz) was applied. In Fig. 8(b), a screenshot showing an example of voltage and current waveforms is presented. A further low-pass filter (f_c = 25 kHz) was applied in post-processing of the experimental data to better clean the waveforms. The instantaneous current ripple is calculated as the difference between instantaneous and fundamental current components, according to (7)

$$\tilde{i}(t) = i(t) - I_{fund}(t). \tag{41}$$

As in previous sections, the first phase was analyzed in the experimental tests, and different values of the modulation index (1/3, 1/2, 2/3, 1, and $2/\sqrt{3} = m_{\max}$) were investigated to cover all the considered cases.

The comparison between the experimental instantaneous current ripple and the peak-to-peak current ripple amplitude evaluated by the equations given in Section III is presented in Fig. 9, for one fundamental period and different modulation indexes (m = 1/3, 1/2, 2/3, 1).

Fig. 10 shows the experimental instantaneous output current (pink trace) compared with the current envelope (blue traces) calculated by combining peak-to-peak current ripple amplitude and fundamental current component, considering the same modulation indexes as in Fig. 9 (m = 1/3, 1/2, 2/3, 1).

The case of the maximum modulation index ($m = 2/\sqrt{3}$) is separately depicted in Fig. 11.

For all the considered cases the agreement between experimental results and analytical developments is good in the whole fundamental period, even if the dead-time effects are not compensated. Since the selected modulation indexes cover all the identified sub-cases (different coloured regions in Fig. 3(c)), the validity of the proposed analysis is proved.

V. CONCLUSION

The analytical evaluation of peak-to-peak output current ripple amplitude in three-phase three-level inverters has been derived in this paper. In particular, the ripple amplitude has been expressed as function of the modulation index in the whole fundamental period of the output voltage, considering centred symmetrical PWM. In addition, a simplified way to readily evaluate the approximate maximum value of the current ripple amplitude is given. The results obtained in all the identified cases have been verified by experimental tests carried out on a custom-made NPC three-level inverter supplying an induction motor. The agreement between experiment results and analytical developments is good in the whole fundamental period, for all the relevant considered cases, proving the validity of the proposed approach. Although the developments have been carried out specifically for symmetrical centered PWM, they can be similarly extended to discontinuous and/or asymmetrical modulations.

VI. REFERENCES

[1] Malinowski, M., Gopakumar, K., Rodriguez, J., Pérez, M.A.: 'A survey on cascaded multilevel inverters', *IEEE Trans. on Industrial Electronics*, July 2010, **57**, (7), pp. 2197 – 2206

[2] Lee, Y.H., Kim, D.H., Hyun, D.S.: 'Carrier based SVPWM method for multi-level system with reduced HDF', Industry Applications Conference, Rome (IT), 8-12 Oct. 2000, pp. 1996-2003

[3] Casadei, D., Serra, G., Tani, A., Zarri, L.: 'Cascaded three-level inverter modulation strategies: a unifying point of view based on duty-cycle space vector approach', International Symposium on Power Electronics, Electrical Drives, Automation and Motion (SPEEDAM), Taormina (IT), 23-26 May 2006, pp. 583 – 590

[4] Zhang, X., Spencer, J.: 'Study of multisamled multilevel inverters to improve control performance', *IEEE Trans. on Power Electronics*, November 2012, **27**, (11), pp. 4409 – 4416

[5] Vafakhah, B., Salmon, J., Knight, A.M.: 'A New Space-Vector PWM With Optimal Switching Selection for Multilevel Coupled Inductor Inverters', *IEEE Trans. on Ind. Electronics*, July 2010, **57**, (7), pp. 2354 – 2364

[6] Wei, S., Wu, B., Li, F., Liu, C.: 'A General Space Vector PWM Control Algorithm for Multilevel Inverters', In Proc. of 18th IEEE Annual IEEE Applied Power Electronics Conference and Exposition (APEC), Miami Beach (FL), 9-13 Feb. 2003, Vol. 1, pp. 562 – 568

[7] Loh, P.C., Holmes, D.G., Fukuta, Y., Lipo, T.A.: 'Reduced common-mode modulation strategies for cascaded multilevel inverters', *IEEE Trans. on Ind. Applications*, Sept/Oct. 2003, **39**, (5), pp 1386 – 1395

[8] McGrath, B.P., Holmes, D.G., Lipo, T.A.: 'Optimized space vector switching sequences for multilevel inverters', *IEEE Trans. on Power Electronics*, Nov. 2003, **18**, (6), pp 1293 – 1301

[9] Bruckner, T., Holmes, D.G.: 'Optimal pulse-width modulation for three-level inverters', *IEEE Trans. on Power Electronics*, January 2005, **20**, (1), pp. 82 - 89

[10] McGrath, B.P., Holmes, D.G., Meynard, T.: 'Reduced PWM harmonic distortion for multilevel inverters operating over a wide modulation range', *IEEE Trans. on Power Electronics*, July 2006, **21**, (4), pp. 941 – 949

[11] Wang, F.: 'Sine-triangle versus space-vector modulation for three-level PWM voltage-source inverters', *IEEE Trans. on Industry Applications*, March/April 2002, **38**, (2), pp. 500 – 506

[12] Yao, W., Hu, H., Lu, Z.: 'Comparison of space-vector modulation and carrier-based modulation of multilevel inverter', *IEEE Trans. on Power Electronics*, January 2008, **23**, (1), pp. 45 – 51

[13] Das, S., Narayanan, G.: 'Novel switching sequences for a space-vector-modulated three-level inverter', *IEEE Trans. on Ind. Electronics*, March 2012, **59**, (3), pp. 1477 – 1487

[14] Srinivas, S., Ramachandra Sekhar, K.: 'Theoretical and experimental analysis for current in a dual-inverter-fed open-end winding induction motor drive with reduced switching PWM', *IEEE Trans. on Ind. Electronics*, October 2013, **60**, (10), 4318 – 4328

[15] Jiang, D., Wang, F.: 'Current-ripple prediction for three-phase PWM converters', *IEEE Trans. on Ind. Applications*, Jan/Feb 2014, **50**, 531 – 538

[16] Grandi, G., Loncarski, J.: 'Evaluation of current ripple amplitude in three-phase PWM voltage source inverters', In Proc. of 8th IEEE International Conference-Workshop on Compatibility and Power Electronics (CPE), Ljubljana (SLO), 5-7 June 2013

[17] Grandi, G., Loncarski, J.: 'Evaluation of current ripple amplitude in five-phase PWM voltage source inverters', In Proc. of IEEE Conference on ICT, Power engineering, and Signal processing (EUROCON), Zagreb (CRO), 1-4 July 2013

[18] Grandi, G., Loncarski, J.: 'Analysis of Peak-to-Peak Current Ripple Amplitude in Seven-Phase PWM Voltage Source Inverters', *Energies*, 2013, **6**, ISSN 1996-1073

[19] Grandi, G., Loncarski, J., Rossi, C.: 'Comparison of Peak-to-Peak Current Ripple Amplitude in Multiphase PWM Voltage Source Inverters', In Proc. of 15th IEEE Conference on Power Electronics and Applications (EPE'13 ECCE Europe), Lille (FR), 3-5 Sept. 2013

[20] Grandi, G., Loncarski, J., Seebacher, R.: 'Effects of Current Ripple on Dead-Time Analysis of Three-Phase Inverters', Proc. of IEEE Energy Conference (ENERGYCON), Florence (IT), 9-12 Sept. 2012, pp. 207 – 212

[21] Herran, M.A., Fischer, J.R., Gonzalez, S.A., Judewicz, M.G., Carrica, D.O.: 'Adaptive dead-time compensation for grid-connected PWM inverters of single-stage PV systems', *IEEE Trans. on Power Electronics*, June 2013, **28**, (6), pp. 2816–2825

[22] Schellekens, J.M., Bierbooms, R.A.M., Duarte, J.L.: 'Dead-time compensation for PWM amplifiers using simple feed-forward techniques', In Proc. of 19th Int. Conference on Electrical Machines (ICEM), Rome, Italy, 6-8 Sept, 2010, pp. 1–6

[23] Ho, C. N. M., Cheung, V.S.P., Chung, H.S.H.: 'Constant-frequency hysteresis current control of grid-connected VSI without bandwidth control', *IEEE Trans. on Power Electronics*, Nov. 2009, **24**, (11), pp. 2484 – 2495

[24] Holmes, D.G., Davoodnezhad, R., McGrath, B.P.: 'An improved three-phase variable-band hysteresis current regulator', *IEEE Trans. on Power Electronics*, Jan. 2013, **28**, (1), pp. 441–450

[25] Jiang, D., Wang, F.: 'Variable Switching Frequency PWM for Three-Phase Converters Based on Current Ripple Prediction', *IEEE Trans. on Power Electronics*, Nov. 2013, **28**, (11), pp. 4951–4961

[26] Srikanthan, S., Mishra, M.K., Rao, R.K.V.: 'Improved hysteresis current control of three-level inverter for distribution static compensator application', *IET Power Electronics*, Sept. 2009, **2**, (5), pp. 517 – 526

[27] Shukla, A., Ghosh, A., Joshi, A.: 'Hysteresis modulation of multilevel inverters', *IEEE Trans. on Power Electronics*, May 2011, **26**, (5), pp. 1396 –1409

[28] Zare, F., Zabihi, S., Ledwich, G.: 'An adaptive hysteresis current control for a multilevel inverter used in an active power filter', European Conference on Power Electronics and Applications, 2-5 Sept. 2007, pp. 1 –8

[29] Grandi, G., Loncarski, J.: 'Simplified implementation of optimised carrier-based PWM in three-level inverters', *IET Electronics Letters*, 2009, 50, (8), pp. 631–633

TABLES

TABLE 1: Duty-cycles for triangles in the first quadrant as function of normalised voltages

	δ_1	δ_2	δ_p
I-1a	$1-\frac{3}{2}\left(u_\alpha+1/\sqrt{3}u_\beta\right)$	$\sqrt{3}\,u_\beta$	$\frac{3}{2}\left(u_\alpha-1/\sqrt{3}u_\beta\right)$
I-1b	$\frac{3}{2}\left(u_\alpha-1/\sqrt{3}u_\beta\right)$	$1-\frac{3}{2}\left(u_\alpha+1/\sqrt{3}u_\beta\right)$	$\sqrt{3}\,u_\beta$
II-1a	$1-\sqrt{3}u_\beta$	$\frac{3}{2}\left(1/\sqrt{3}\,u_\beta-u_\alpha\right)$	$\frac{3}{2}\left(u_\alpha+1/\sqrt{3}u_\beta\right)$
I-2a	$\frac{3}{2}\left(u_\alpha+1/\sqrt{3}u_\beta\right)-1$	$1-\frac{3}{2}\left(u_\alpha-1/\sqrt{3}u_\beta\right)$	$1-\sqrt{3}\,u_\beta$
I-2b	$1-\sqrt{3}u_\beta$	$\frac{3}{2}\left(u_\alpha+1/\sqrt{3}u_\beta\right)-1$	$1-\frac{3}{2}\left(u_\alpha-1/\sqrt{3}u_\beta\right)$
II-2a	$1-\frac{3}{2}\left(u_\alpha+1/\sqrt{3}u_\beta\right)$	$\sqrt{3}u_\beta-1$	$1-\frac{3}{2}\left(1/\sqrt{3}u_\beta-u_\alpha\right)$
I-3a	$\sqrt{3}u_\beta$	$\frac{3}{2}\left(u_\alpha-1/\sqrt{3}u_\beta\right)-1$	$2-\frac{3}{2}\left(u_\alpha+1/\sqrt{3}u_\beta\right)$
I-3b	$\sqrt{3}u_\beta-1$	$\frac{3}{2}\left(u_\alpha-1/\sqrt{3}u_\beta\right)$	$2-\frac{3}{2}\left(u_\alpha+1/\sqrt{3}u_\beta\right)$
II-3a	$\frac{3}{2}\left(1/\sqrt{3}u_\beta-u_\alpha\right)$	$\frac{3}{2}\left(u_\alpha+1/\sqrt{3}u_\beta\right)-1$	$2-\sqrt{3}u_\beta$

TABLE 2: Determination of common-mode voltage in the different cases [11]

Conditions	CM
Mid < 0 & (*Max* - *Min*) > 1	*Min*/2
Mid > 0 & (*Max* - *Min*) < 1	*Max*/2
Mid < 0 & (*Max* - *Min*) > 1 & (1 - *Max*) > - *Mid*	- (1 - *Max*)/2
Mid > 0 & (*Max* - *Min*) > 1 & (1 + *Min*) > *Mid*	(1 + *Min*)/2
Others	-(*Max* + *Min*)/2

FIGURES

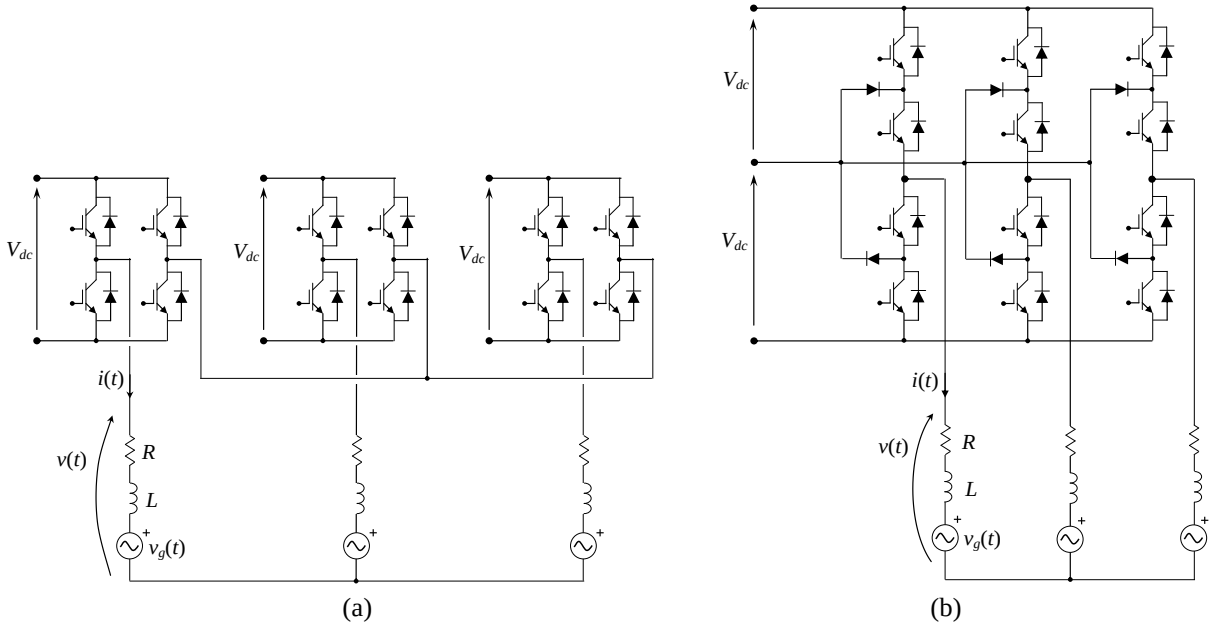

Fig. 1. Three-level inverter supplying an RLE circuit, representing either a motor-load or a grid-connected application: (a) H-bridge and (b) NPC configurations.

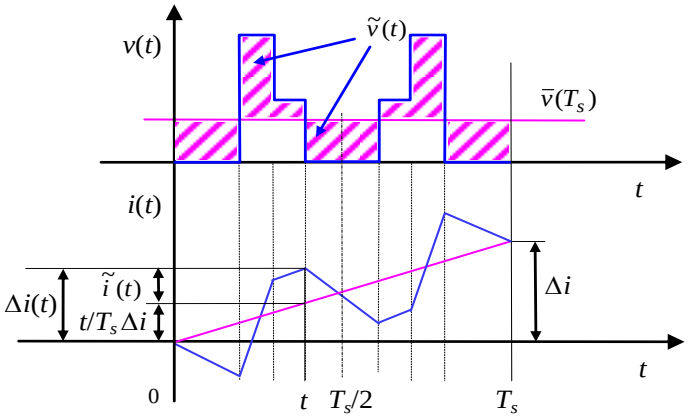

Fig. 2. Example of voltage and current supplied by the inverter in a switching period.

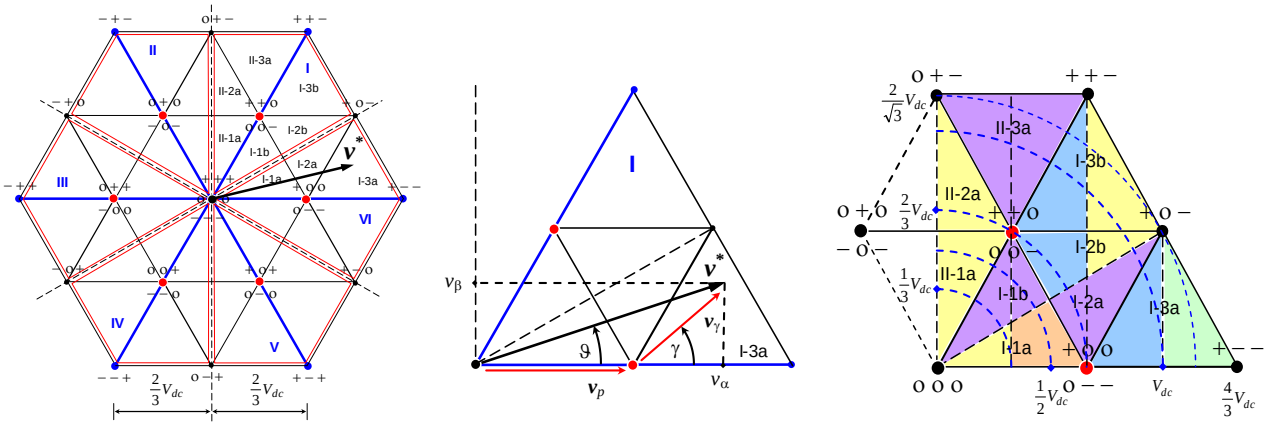

Fig. 3. Space vector diagrams of inverter output voltage: (a) whole hexagon with all six main triangles, (b) detail of first main triangle, (c) areas identified for ripple evaluation in the first quadrant, blue dashed circles represent the cases with m = 1/3, 1/2, 2/3, 1, $2/\sqrt{3}$ (m_{max}).

Pre-print. Final version of this paper appears inIET Digital Library (http://digital-library.theiet.org/content/journals/iet-pel) and IEEE Xplore Digital Library (http://ieeexplore.ieee.org/Xplore/guesthome.jsp).

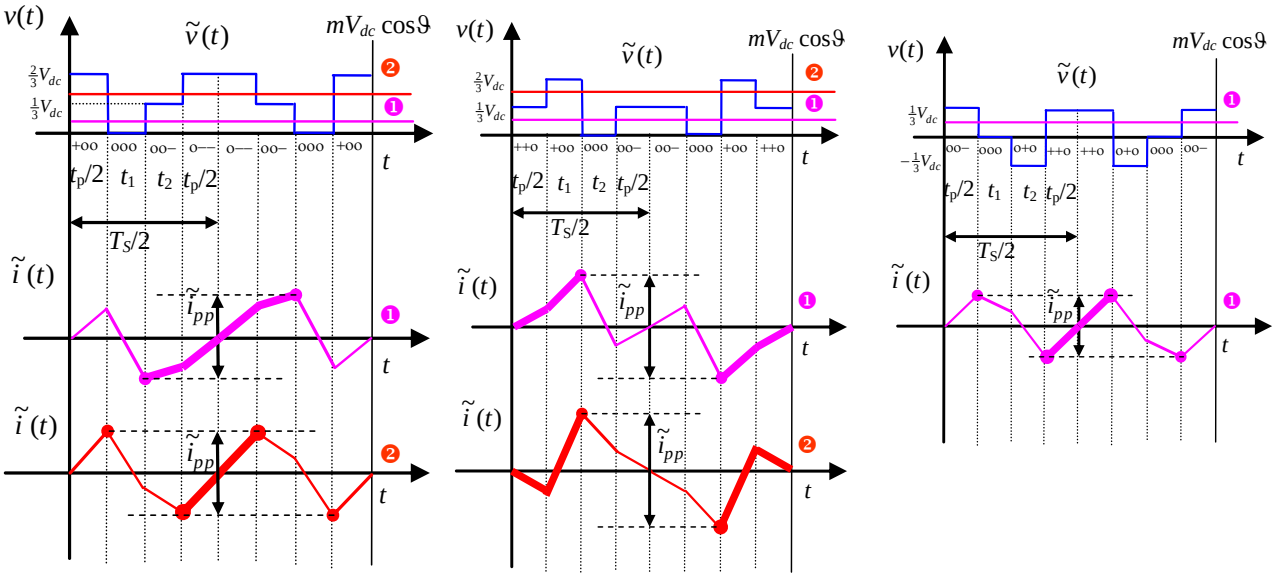

(a) triangle I-1a (b) triangle I-1b (c) triangle II-1a

Fig. 4. Inner triangles: instantaneous output voltage $v(t)$, current ripple $\tilde{i}$ and peak-to-peak value $\tilde{i}_{pp}$.

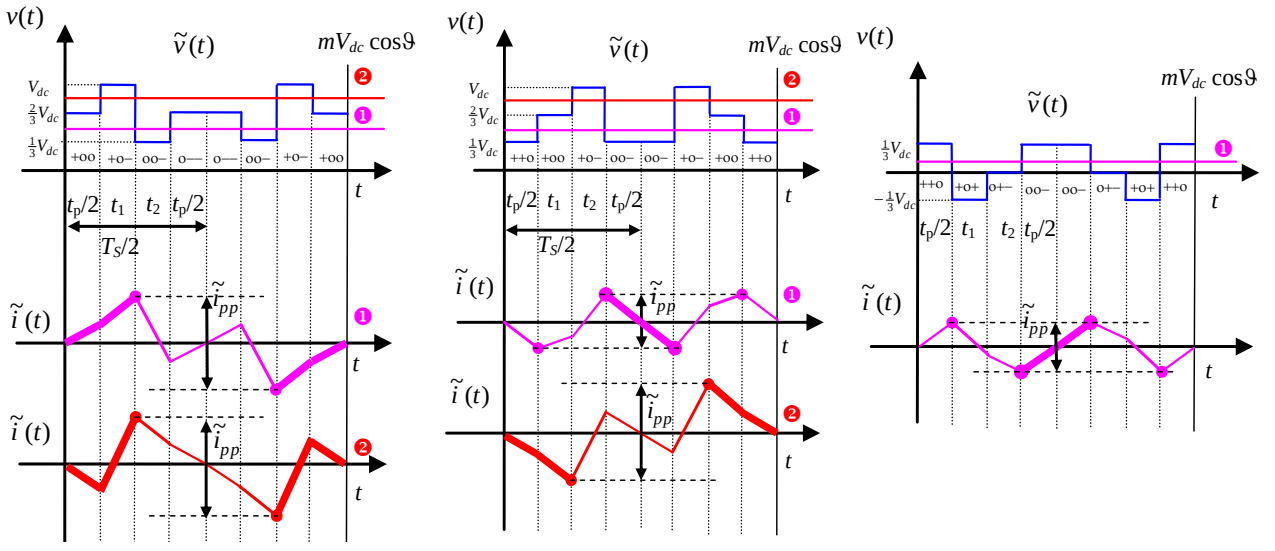

(a) triangle I-2a (b) triangle I-2b (c) triangle II-2a

Fig. 5. Intermediate triangles: instantaneous output voltage $v(t)$, current ripple $\tilde{i}$ and peak-to-peak value $\tilde{i}_{pp}$.

Pre-print. Final version of this paper appears inIET Digital Library (http://digital-library.theiet.org/content/journals/iet-pel) and IEEE Xplore Digital Library (http://ieeexplore.ieee.org/Xplore/guesthome.jsp).

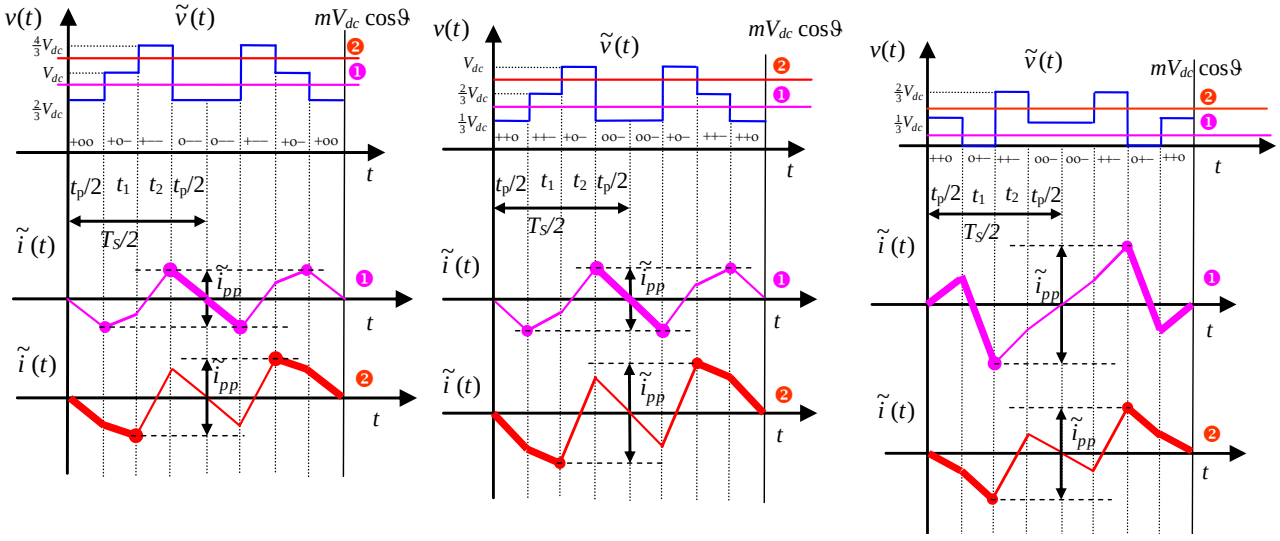

(a) triangle I-3a (b) triangle I-3b (c) triangle II-3a

Fig. 6. Outer triangles: instantaneous output voltage $v(t)$, current ripple $\tilde{i}$ and peak-to-peak value $\tilde{i}_{pp}$.

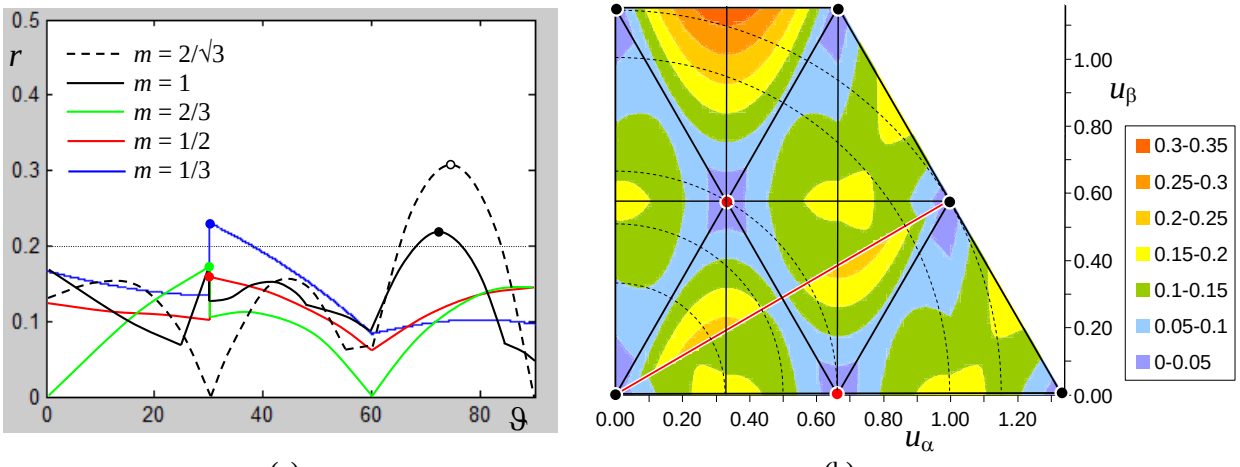

(a) (b)

Fig. 7. Normalized peak-to-peak current ripple amplitude $r(m,\vartheta)$ in the first quadrant:

(a) for different modulation indexes as a function of ϑ, (b) as a coloured map in the normalized voltage plane α-β.

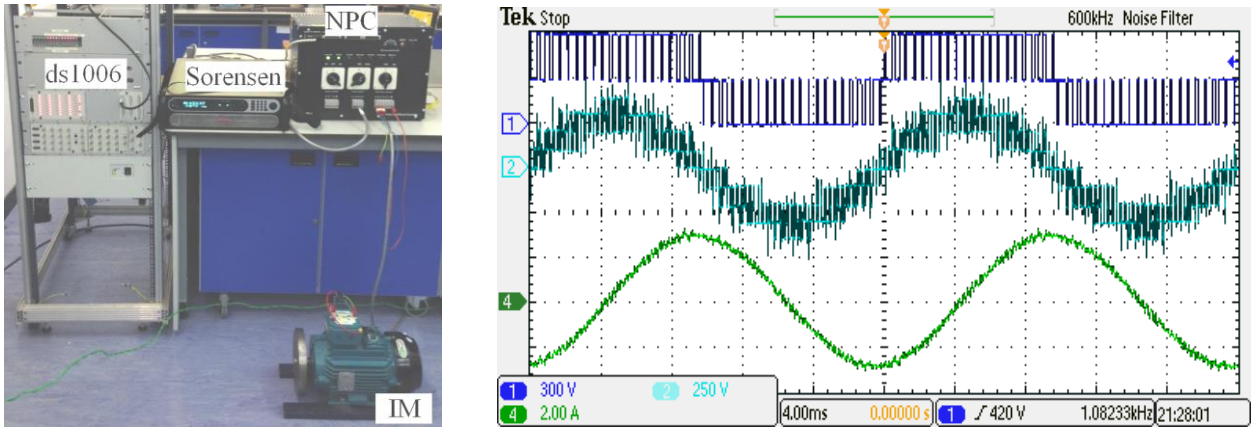

(a) (b)

Fig. 8. (a) Experimental setup and (b) example of output voltage and current waveforms from the scope.

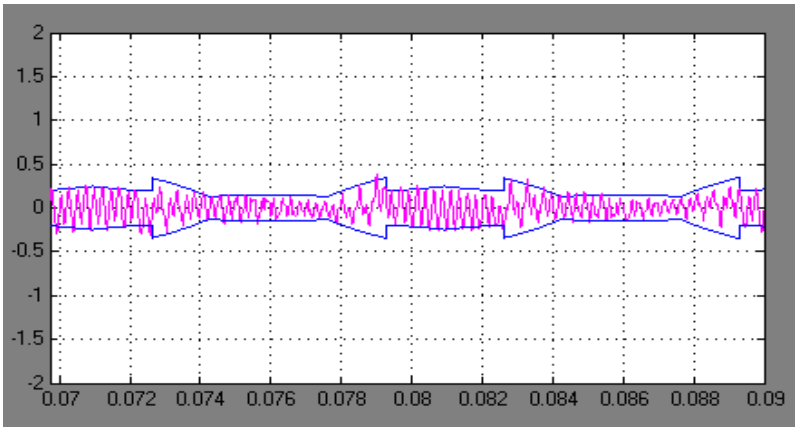

(a) m = 1/3

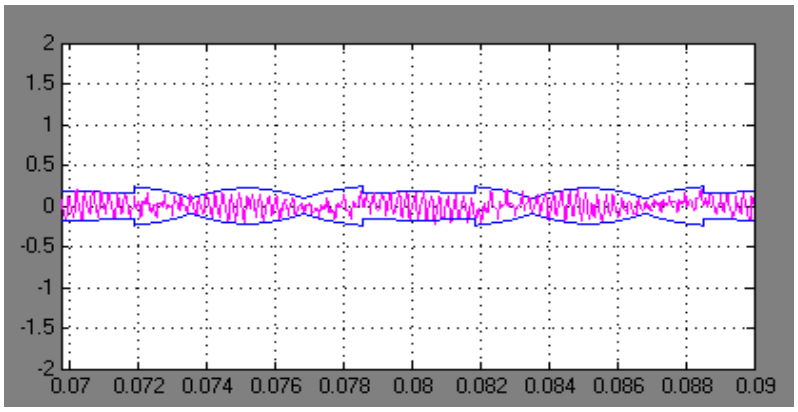

(b) m = 1/2

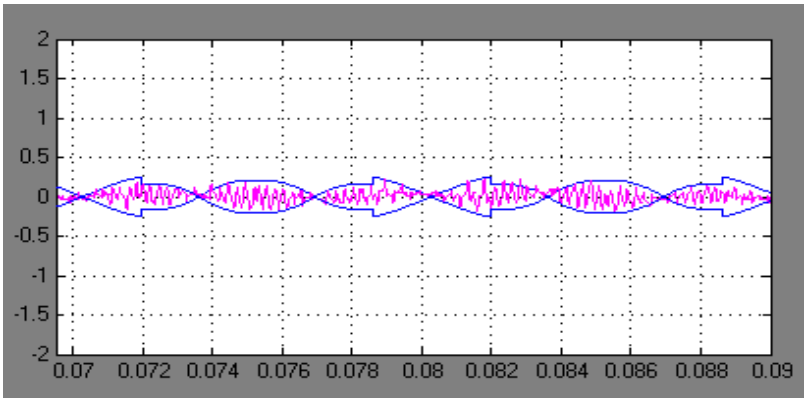

(c) m = 2/3

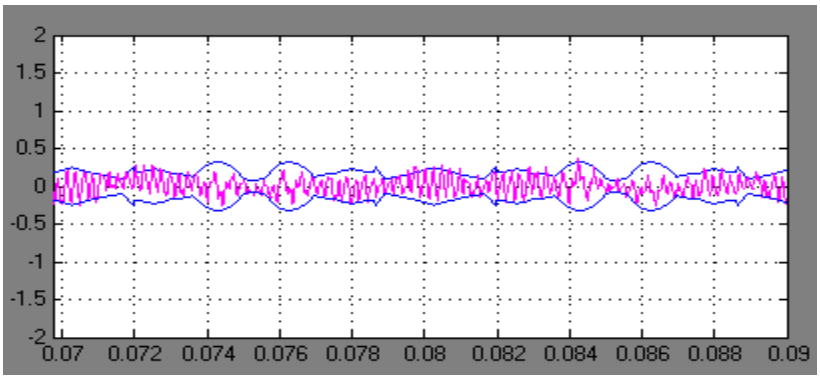

(d) m = 1

Fig. 9. Comparison between experimental current ripple (pink traces) and calculated peak-to-peak envelope (blue traces) in the fundamental period, for different modulation indexes.

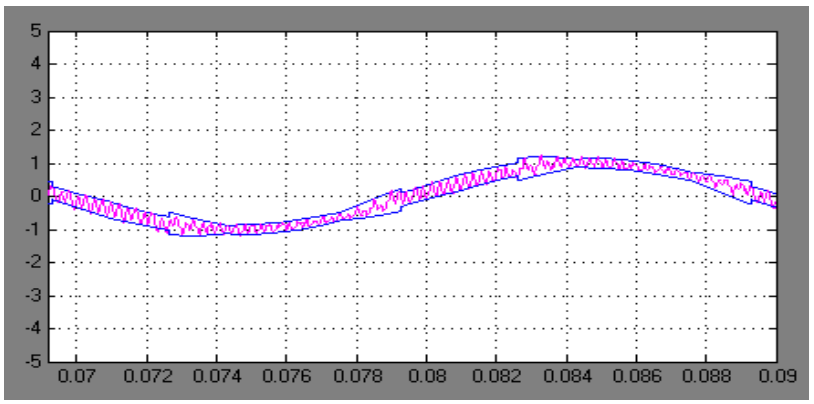

(a) m = 1/3

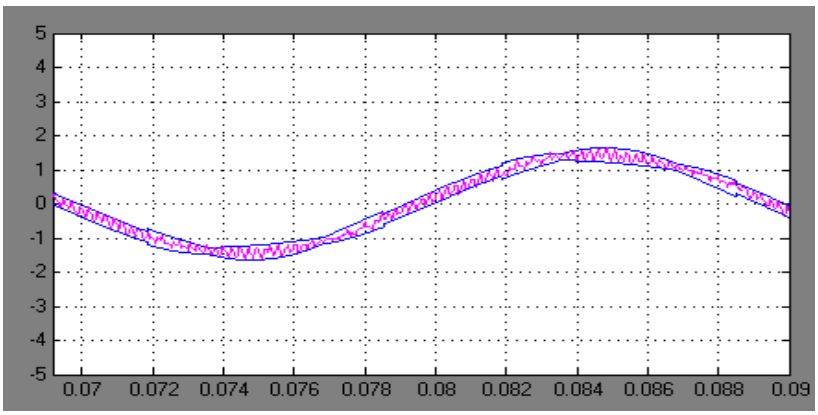

(b) m = 1/2

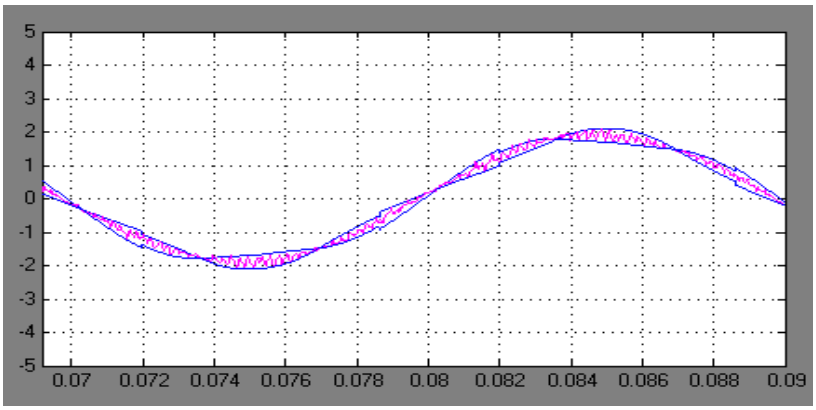

(c) m = 2/3

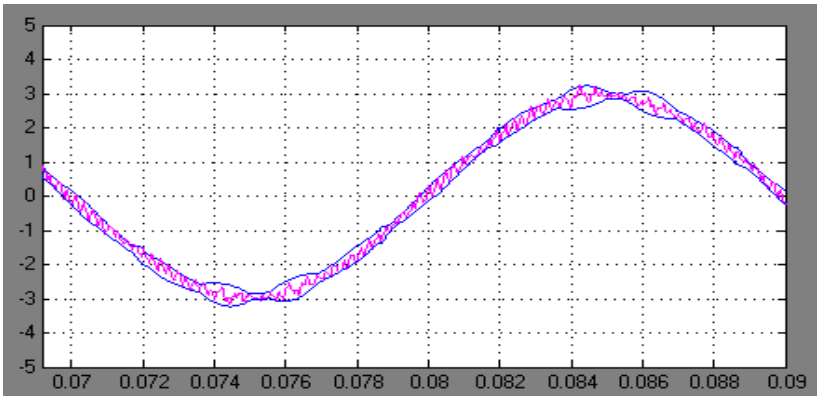

(d) m = 1

Fig. 10. Comparison between experimental instantaneous current (pink traces) and calculated current envelope (blue traces) in the fundamental period, for different modulation indexes.

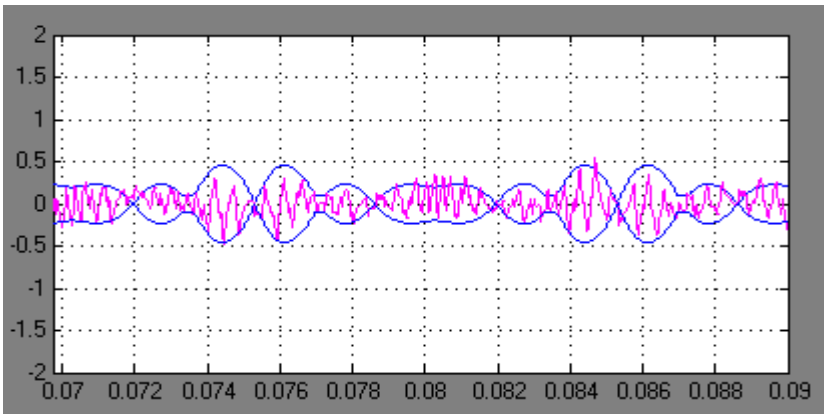

(a)

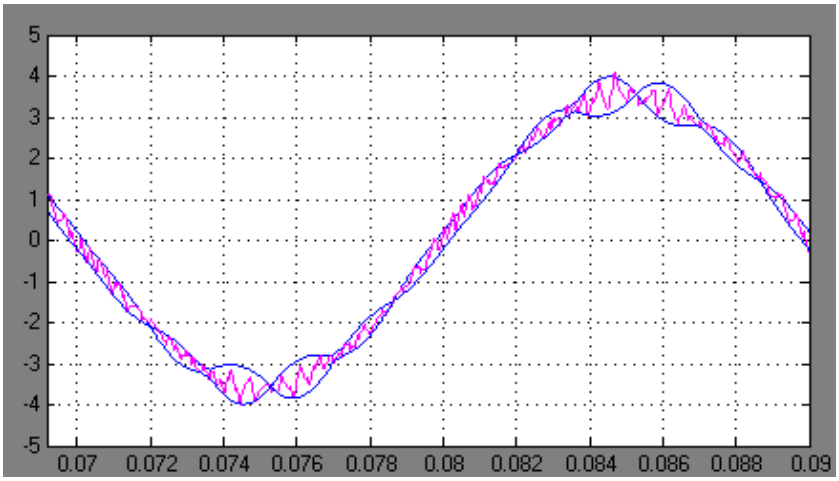

(b)

Fig. 11. Comparison between experimental (pink) and analytical results (blue) in the fundamental period with maximum modulation index, $m = 2/\sqrt{3}$: (a) experimental current ripple and calculated peak-to-peak amplitude, (b) experimental instantaneous current and calculated current envelope.